

# Preparation of Core-shell Structure Carbon@SnM<sub>2</sub> (M=S, O) Microspheres Composites and Application in Lithium-ion Batteries

Ansong Wang<sup>1</sup>, Penglin Zhang<sup>1</sup>, Xiujuan Chen<sup>2,\*</sup> and Guoyun Yu<sup>1</sup>

<sup>1</sup> State Key Laboratory of Advanced Processing and Recycling of Nonferrous Metals, Lanzhou University of Technology, Lanzhou 730050, China

<sup>2</sup> College of Mechano-Electronic Engineering, Lanzhou University of Technology, Lanzhou 730050, China

\*E-mail: [chenxj@lut.cn](mailto:chenxj@lut.cn)

Received: 4 January 2019 / Accepted: 31 January 2019 / Published: 10 March 2019

---

We report a fast solvothermal approach to fabricate the core-shell structure carbon@SnS<sub>2</sub> microspheres composites (C@SnS<sub>2</sub>). And the same structured carbon@SnO<sub>2</sub> microspheres composites (C@SnO<sub>2</sub>) were synthesized by calcinating of C@SnS<sub>2</sub> at 500°C in air. Then the phase structures and the morphologies of the carbon@SnM<sub>2</sub> (M=S, O) microspheres composites (C@SnM<sub>2</sub>) were observed by X-ray diffraction analysis (XRD), scanning electron microscopy (SEM) and transmission electron microscopy (TEM). The C@SnM<sub>2</sub> were composed of the uniform micron-sized carbon spheres with 1.5 μm as the core and SnM<sub>2</sub> with 200 nm as the shell. When putting it as the anode electrodes of lithium-ion batteries, the C@SnS<sub>2</sub> showed higher charge/discharge capacity, rate capability and cycling reversibility than C@SnO<sub>2</sub>. Those excellent electrochemical performances make the C@SnS<sub>2</sub> to be a predominated candidate for the lithium-ion batteries.

---

**Keywords:** SnS<sub>2</sub>; SnO<sub>2</sub>; core-shell structure; anode materials; lithium-ion batteries.

## 1. INTRODUCTION

In the last few decades, energy crisis and environmental pollution are common problems faced by the world, which is closely related to the health of the people, the global environment and the economy. Therefore, those problems have drawn researchers more attention and have been put more stress on, and are pushing researchers to develop the clean, effective and sustainable technologies to supply and store energy. Among the various technologies, electrochemical energy storage devices are considered as the most feasible environmentally friendly and sustainable devices [1]. Currently

lithium-ion batteries (LIBs) are the prevailing energy storage device over the kinds of electrochemical energy storage equipments.

In the past few years more and more anode materials of LIBs appeared, such as carbonaceous materials, silicon-based materials, antimony-based materials, tin-based materials, metallic sulfide and so on. In the above materials, metallic sulfide can be widely used in LIBs as well as lithium-sulfur batteries while there are also many differences between the two types of batteries. Table 1 shows the comparison of the two types of batteries. The tin-based anode electrodes are considered to be the most predominate candidates which can displace the conventional graphite (370 mAh/g) on account of their high theoretical specific capacity (992 mAh/g) [2]. Therefore, the tin-based materials and their composites in various morphologies and structures have been inquired as the anode electrodes of LIBs. Recently, a great deal of researches have concentrated in developing both simple and special approaches for fabricating novel structures to investigate their extraordinary properties to enhance electrochemical properties of LIBs [3].

**Table 1.** the comparison between lithium-ion batteries and lithium-sulfur batteries

Description	Lithium-ion batteries	Lithium-sulfur batteries.
Cathode materials	LiCoO <sub>2</sub> , LiNiO <sub>2</sub> , LiMn <sub>2</sub> O <sub>4</sub> , LiFePO <sub>4</sub>	lithium metal
Anode materials	transition metal sulfides	elemental sulfur, sulfur based compounds
Reaction mechanism	intercalation mechanism	electrochemical mechanism
Theoretical specific capacity	645 mAh/g as SnS <sub>2</sub>	1675 mAh/g
Operating temperature range	-20-60°C	-40-70°C
Advantages	high electronic conductivity, ideal mechanical stability and thermodynamic stability	low price, environmentally friendly high theoretical energy density
Disadvantages	low lithium ion diffusion rate , passivation of reactive materials	shuttle effect in the process of charge and discharge, volumetric strain, low utilization of active materials

As known, the structure and morphology can greatly influence the electrochemical properties of LIBs. SnS<sub>2</sub> as a layered hexagonal CdI<sub>2</sub>-type structured crystal owns the tight Sn-S covalent bonds in the structure that the octahedral regulative Sn atoms caught between two layers of sulfur atoms [4], which composed by two layers of close-packed sulfur layer with tin layer that caught between them in an octahedral coordination [5-7]. The specific layered sandwich structure (greater than the layer spacing of 0.37 nm) facilitates the intercalation and deintercalation of lithium ions. Even though SnS<sub>2</sub>

presents high theoretical capacity (645 mAh/g), the severe effect of volumetric expansion and loss of electrical contact during lithium intercalation and deintercalation resulted in capacity fading of the compound [8]. The other tin-based anode materials-tin oxides ( $\text{SnO}_2$ ) possessed higher theoretical capacity (782 mAh/g) than  $\text{SnS}_2$  have also been investigated comprehensively [9]. When applied as the typical n-type wide gap semiconductor,  $\text{SnO}_2$  has been widely used in gas sensors, catalyst, solar cells, photo detectors and LIBs [10-15]. But, the  $\text{SnO}_2$  mainly suffer from the following problems when put it as anode materials in LIBs, which are similar to pure  $\text{SnS}_2$  anodes: (i) the severe effect of volumetric expansion (ii) the poor electronic conductivity [16].

Nowadays, the key factors to perfect the electrochemical performance of tin-based anode electrodes of LIBs are to buffer the volume changes, reduce aggregation problem meanwhile promote the electronic conductivity of the materials. Numerous efforts discovered that the carbon-coated maybe a predominating approach to solve those problems. This is because the carbon in the composites works as a barrier to disperse the aggregation of active particles as well as strengthen their structural stability during in the process of charge and discharge. In addition, carbon possesses a high electronic conductivity that can improve the conductance of the composites electrodes. For instance, the electrochemical analyzes of  $\text{SnO}_2$  [17-20],  $\text{TiO}_2$  [21, 22],  $\text{Fe}_3\text{O}_4$  [23, 24],  $\text{Co}_3\text{O}_4$  [25, 26], and  $\text{NiO}$  [27, 28] had been substantially improved modified by carbon coating. As a consequent, the fabrication of composite electrodes modified by carbon is a valid method to enhance the electrochemical performance of electrodes. However, there was a few of studies have been covered the application of tin-based electrodes anchoring on the carbon microspheres.

Herein, we demonstrate a core-shell structure of carbon @ $\text{SnM}_2$  ( $\text{M}=\text{S}, \text{O}$ ) microspheres composites ( $\text{C@SnM}_2$ ) as anode materials of LIBs. In this unique hybrid structure,  $\text{SnM}_2$  compounds are anchored on carbon microspheres (Cs) surfaces as anode materials. When putting  $\text{C@SnM}_2$  ( $\text{M}=\text{S}, \text{O}$ ) as the anode materials of LIBs possess the following advantages: (i) the distinctive core-shell structure are designed not only does buffer the volume changes of  $\text{SnM}_2$  effectively, but also can effectively alleviate aggregation of  $\text{SnM}_2$  (ii) as serving the conductive phases, Cs can improve the electrical conductivity and electrochemical stability of pure  $\text{SnM}_2$  ( $\text{M}=\text{S}, \text{O}$ ) anode materials. Consequently, the produced composites exhibit the better performances as the anode materials for LIBs.

## 2. EXPERIMENT SECTION

### 2.1 Fabrication of the carbon microspheres (Cs)

The carbon microspheres were fabricated by one-step facile hydrothermal synthesis as described for the previous report [29]. In the synthesized procedure, the given mass of sucrose was added in 60 mL distilled water stirred until dissolved at the room temperature to obtain the 0.3 M sucrose aqueous solution. Subsequently, the sucrose aqueous solution was put into a 100 mL Teflon-lined stainless steel autoclave and heat treated at  $180^\circ\text{C}$  for 4 h. After cooled down, the product precipitates were washed by deionized water and ethanol several times alternatively till the upper layer

being colorless, transparent and the solid-liquid separated by centrifugation. Finally, the acquired samples were oven-dried at 70°C for 9 h.

## 2.2 Fabrication of the core-shell carbon @ SnM<sub>2</sub> (M=S, O) microspheres composites (C@SnM<sub>2</sub>)

In order to synthesize carbon @ SnM<sub>2</sub> (M=S, O) microspheres, the solvothermal method was used to gain the destination products. In the synthesized procedure, 0.1 g as-prepared Cs were added in 20 mL ethanol solution, then stirred for 1 h until well combined. Next, 20 mL ethanol composites contained with 20 mg Cs were put into a 40 mL ethanol solution which contained 5 mmol **SnCl<sub>4</sub>5H<sub>2</sub>O** and 10 mmol thioacetamide (Sn:S=1:2) that stirred well for 1 h at room temperature. Subsequently, the mixed solution was put into a 100 mL Teflon-lined stainless steel autoclave and solvothermal treated at 160°C for 6 h and then cooled down naturally. The obtained precipitates were collected by centrifugation and washed by distilled water and ethanol repeatedly. Finally, the C@SnS<sub>2</sub> composites were dried in vacuum oven at 70°C for 9 h. The C@SnO<sub>2</sub> products were acquired by thermally treated the as-prepared C@SnS<sub>2</sub> in the air at 500°C for 3 h in an electrical furnace.

## 2.3 Material characterization

The phase structures of the products were tested by the X-ray diffraction (XRD) by the Cu Ka radiation on Rigaku D/Max-2400 with gathered in  $10^\circ \leq 2\theta \leq 90^\circ$  at a scanning rate of 8°/min. Scanning electron microscopy (SEM) images were observed the morphologies of the products by using a JSM-6700F field emission scanning electron microscope with the operating voltages at 5 kV. Transmission electron microscope (TEM) study was carried out by using the instrument named JSM-6701.

## 2.4 Electrochemical measurement

All of the electrochemical measurements were adopted by the CR2032 coin-type cells. The homogeneous slurry was consisted by the mixing of 80wt% as-prepared carbon @ SnM<sub>2</sub>, 10wt% acetylene black and 10wt% polyvinylidene fluoride (PVDF) binder with a solution of N-methyl-2-pyrrolidone (NMP). Subsequently, the as-prepared slurry was painted on the copper foil current collector. Then the obtained electrodes were dried at 80°C for 12 h in the vacuum oven. As for the prepared cell, it was composed by investigated electrodes, the lithium foil as the counter electrodes and a Celgard2300 microporous polypropylene film as the separator which was assembled in an argon-filled dry glove box.

1 M LiPF<sub>6</sub> in a mixture of 50wt% ethylene carbonate (EC) and 50wt% 1,2-dimethoxyethane which was made as the electrolyte. The electrochemical performances of the prepared cells were recorded through the Land CT2001A battery testing system in a voltage window of 0.1 V to 3.0 V (vs. Li<sup>+</sup>/Li) in different current rates. The cyclic voltammetry (CV) was conducted with a CHI660D electrochemical workstation in a voltage window of 0.01-3.0 V at a scan rate of 0.3 mV/s. And the electrochemical impedance spectra (EIS) were recorded on the same electrochemical workstation by

the frequency range from 0.01 Hz to  $10^5$  Hz with the disturbance amplitude of 5 mV. All electrochemical measurements were carried out at room temperature.

### 3. RESULTS AND DISCUSSION

The crystal structure of the synthesized powder was characterized by X-ray diffraction (XRD). Fig. 1(a) is shown the recorded the XRD pattern of carbon microspheres (Cs): There is one diffraction peaks centered at  $23^\circ$ , which corresponds to (002) diffractions from the graphitic [30]. Meanwhile, the (002) diffraction peak shows broad and low in intensity indicating the randomly oriented graphene layers in the turbostratic carbon structure [31, 32]. The result shows Cs exist as amorphous carbon. Then the morphology of Cs investigated by SEM is shown in Fig. 1(b). The prepared Cs is found to possess good dispersion with a uniform size of  $1.84 \mu\text{m}$ .

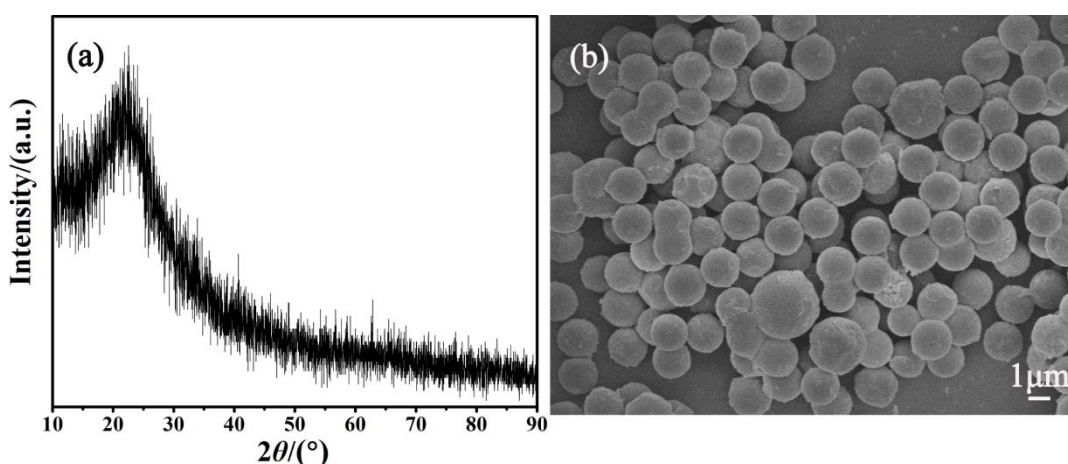


**Figure 1.** XRD pattern and SEM images of Cs sample (a) XRD (b) SEM

The typical XRD pattern of the core-shell structure carbon@ $\text{SnM}_2$  ( $\text{M}=\text{S}, \text{O}$ ) microspheres composites ( $\text{C@SnM}_2$ ) are displayed in Fig. 2. All the reflexes of  $\text{C@SnS}_2$  can be indexed to the pure hexagonal of  $\text{SnS}_2$  (JCPDS no. 23-677). The new appeared peaks are fully compatible with tetragonal  $\text{SnO}_2$  (JCPDS no. 41-144sx5) after calcination in air. In this pattern, none hexagonal phase of  $\text{SnS}_2$  was obtained, indicating the  $\text{SnS}_2$  completely oxidized to the  $\text{SnO}_2$  after calcination. Furthermore, no graphitic carbon reflexes are observed, denoting the amorphous phase in both two samples with low crystallinity and explaining the structures of  $\text{SnS}_2$  and  $\text{SnO}_2$  were not affected by the presence of the Cs. Those results were consistent with those reported in other literature [33-35].

Scanning electron microscopy (SEM) has been used to analyze the morphology of the  $\text{C@SnS}_2$  and  $\text{C@SnO}_2$  composites. Fig. 3(a) (b) illustrate SEM images of the core-shell structured  $\text{C@SnS}_2$  microspheres. As we can see, the particles size of  $\text{C@SnS}_2$  produced is uniform and their average diameters are  $2.0 \mu\text{m}$ . As is shown in Fig. 3(b) the nanosized  $\text{SnS}_2$  sheets developed perfectly on the surfaces of Cs, and on this basis, a good deal of reticular structures are formed the surface of core-shell structures. After calcination in the air, the morphologies of  $\text{C@SnO}_2$  are revealed in Fig. 3(c) (d). Although the  $\text{C@SnO}_2$  composites maintain the original core-shell structure completely as recorded in

Fig. 3(c), the part of the shell has transformed from SnS<sub>2</sub> nanosheets to SnO<sub>2</sub> nanoparticles as observed in Fig. 3(d). This is mainly that the sublimation of oxygen and sulfur makes the sulphur to escape from the tin disulfide nano-sheet due to the C@SnS<sub>2</sub> calcination in air at 500°C.

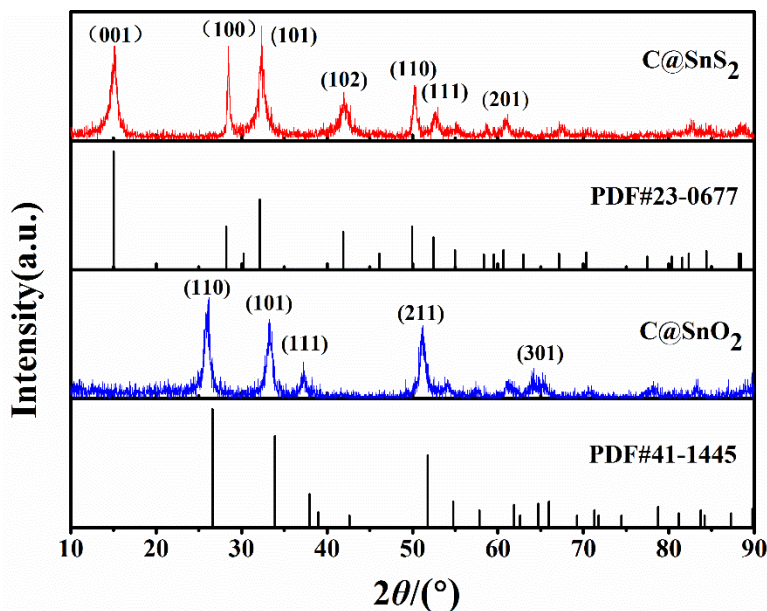


Figure 2. XRD pattern of C@SnS<sub>2</sub> and C@SnO<sub>2</sub> composites

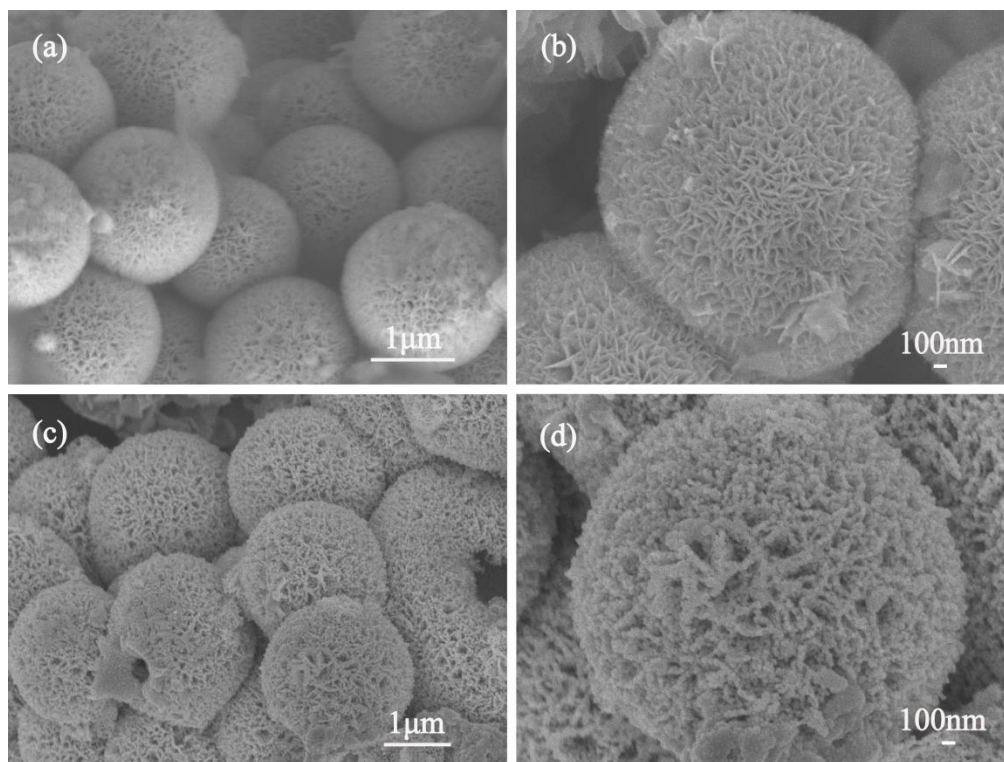
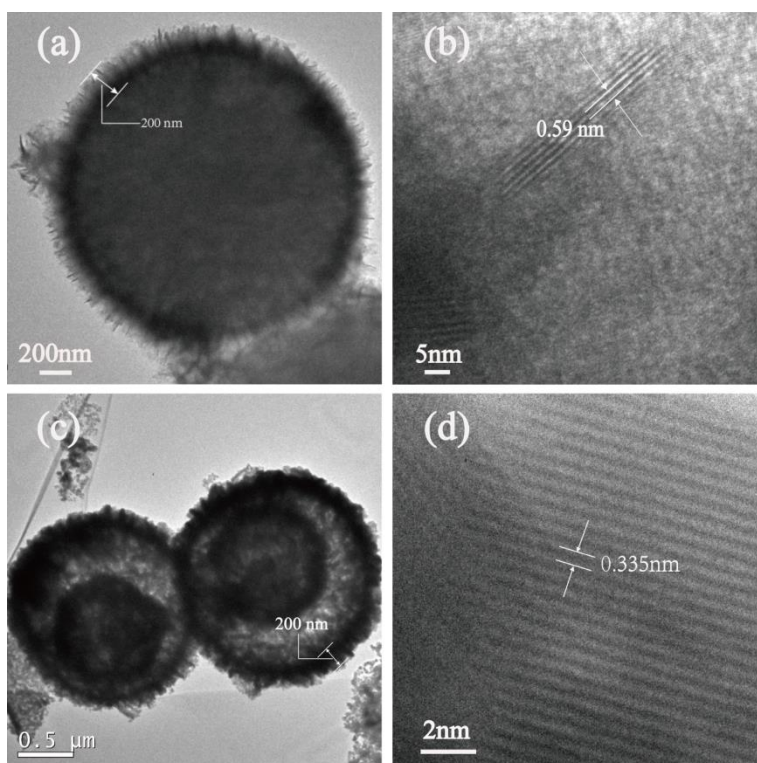


Figure 3. SEM images of different magnification C@SnS<sub>2</sub> and C@SnO<sub>2</sub> composites (a)(b) C@SnS<sub>2</sub> (c)(d) C@SnO<sub>2</sub>

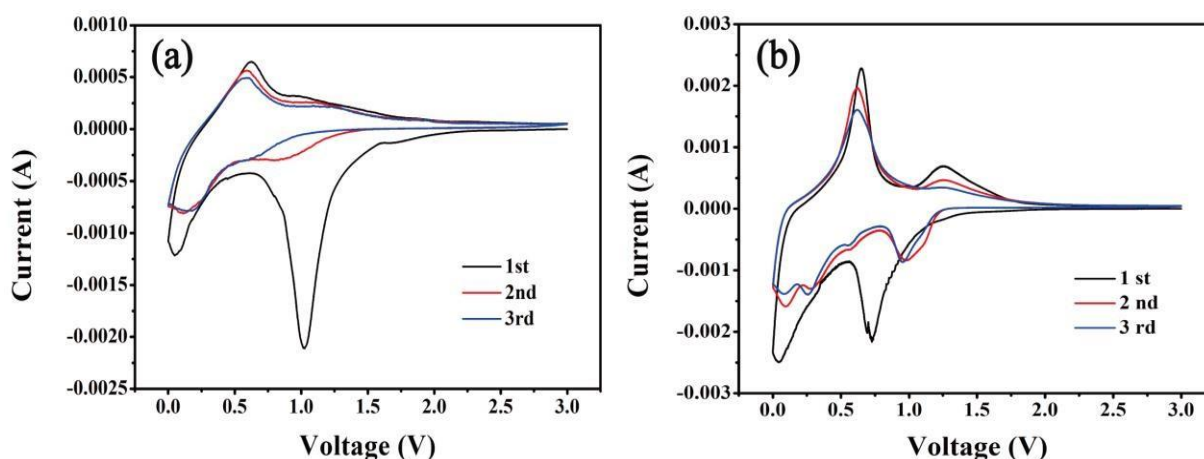
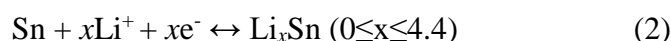
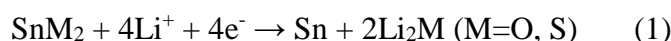
TEM and HRTEM images of the C@SnS<sub>2</sub> and C@SnO<sub>2</sub> composites are shown in Fig. 4. The core-shell structure C@SnS<sub>2</sub> and C@SnO<sub>2</sub> composites are both in well monodispersion as well as good sphericity were investigated in Fig. 4(a) (c), respectively. From those images, it is clearly observed that the particles size of both two core-shell structures composites is about 1.5 μm, and the shell thickness of the both is about 200 nm. This particular core-shell structure has not changed much in the process of calcination. The ultrathin SnS<sub>2</sub> nanosheets as the shell have developed the perfectly uniform thickness on the Cs surface perpendicularly as shown in Fig. 4(a). However, there is a gap between the core of carbon microspheres and the shell of SnO<sub>2</sub> after annealing at 500°C of C@SnS<sub>2</sub> as Fig. 4(c). The reason for this phenomenon is that the part of the carbon from the carbon microspheres escaped as carbon dioxide after heat treatment. Fig. 4(b) (d) illustrates HRTEM images of the edge of the C@SnS<sub>2</sub> and C@SnO<sub>2</sub> composites, respectively. As illustrated in Fig. 4(b), the particular interplanar spacing is calculated to be 0.59 nm as same as the (001) plane of a hexagonal phased SnS<sub>2</sub>. The clear lattice fringes can be investigated in HRTEM images of Fig.4 (d) shows that the C@SnO<sub>2</sub> owns high crystallinity without any the dislocations and stacking faults [36]. The distance between adjacent layers is calculated to be 0.335 nm that represent the (110) planes of tetragonal phased SnO<sub>2</sub>.



**Figure 4.** TEM and HRTEM images of C@SnS<sub>2</sub> and C@SnO<sub>2</sub> composite (a)(b) C@SnS<sub>2</sub> (c)(d) C@SnO<sub>2</sub>

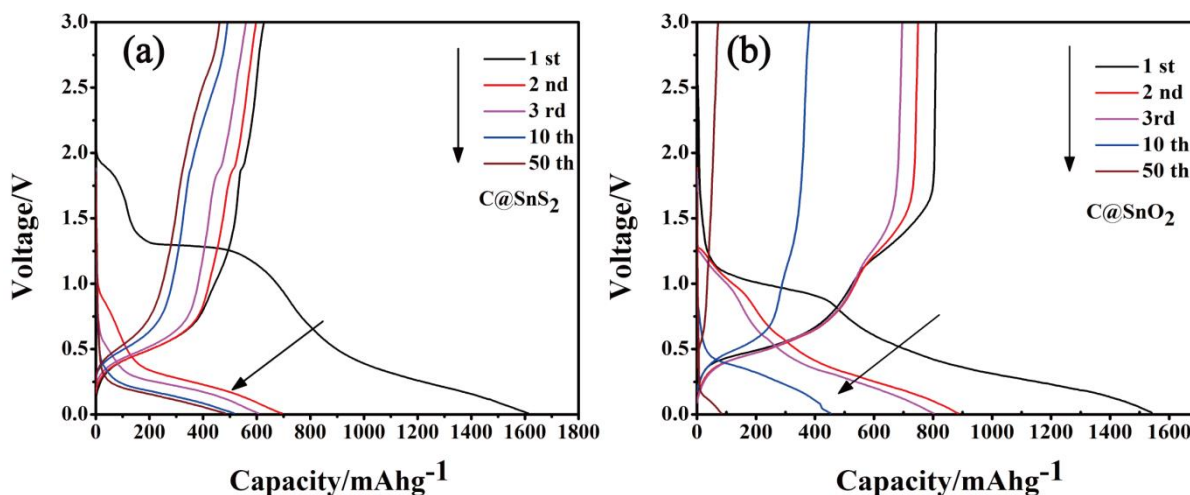
To further elaborate the lithium storage behaviors of C@SnM<sub>2</sub> (M=O, S) composites for lithium-ion batteries (LIBs), the cyclic voltammetry measurements (CV) for the first three cycles are evaluated at a current density of 0.3 mV/s in a voltage window of 0.01-0.3 V as shown in Fig. 5. In the first cathodic scan of the C@SnS<sub>2</sub> in Fig. 5(a), the peak located around 1.75 V is related to the lithium ion intercalated into SnS<sub>2</sub> layers without changes of phase structure [37]. And in the following cycles,

this reduction peak disappears. There was the second reduction peak around 1.1 V ascribing to decomposition of SnS<sub>2</sub> into Sn as well as the formation of Li<sub>2</sub>S and solid electrolyte interface (SEI) film through the Reaction (1). At the anodic sweep, the peaks located around 0.65 V and 1.2 V represent the de-alloying process of Li-Sn alloy and the partial decomposition of Li<sub>2</sub>S, oxidation of Sn as well as the formation of SnS<sub>2</sub>, respectively, which consistent with the earlier literature [38]. As for the core-shell C@SnO<sub>2</sub> composites in Fig. 5(b), there were two characteristic peaks in the first cycle. They were situated at 0.75 V and 0.1 V, which can be account for the decomposition of the SnO<sub>2</sub> into Sn and Li<sub>2</sub>S in Reaction (1) and the formation of Li<sub>x</sub>Sn alloys through the Reaction (2), respectively. Meanwhile, there were two peaks around 0.75 V and 1.3 V can be ascribed to the de-alloying processes of Li-Sn alloys in Reaction (1) and the lithium ions extrude from the SnS<sub>2</sub> with the phase changes [39].



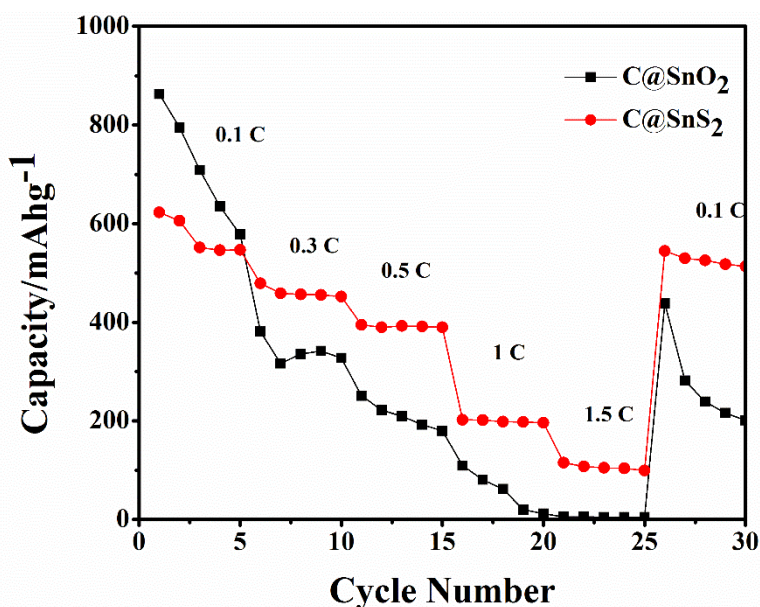
**Figure 5.** CV curves of C@SnS<sub>2</sub> and C@SnO<sub>2</sub> composites (a) C@SnS<sub>2</sub> (b)C@SnO<sub>2</sub>

Fig. 6 records on the charge/discharge profiles of C@SnS<sub>2</sub> and C@SnO<sub>2</sub> composites for the first fiftieth cycle at a current density of 100 mA/g (0.15 C) in voltage windows of 0.01 V-3.0 V. As we can see, during the first discharge curve, three plateaus present at approximately 1.8V, 1.2 V and 0.2 V of C@SnS<sub>2</sub> sample in Fig. 6(a) and two plateaus around 0.75 V and 0.1 V are discovered of C@SnO<sub>2</sub> sample in Fig. 6(b). These discharge platforms in the first discharge curve of both two samples are accord with the mentioned CV curve in Fig. 5, respectively. At the same time, the irreversible capacity loss in the first cycle occurred at both products suggest the formation of solid electrolyte interphase (SEI) films of the anode electrodes [40]. The initial discharge and charge capacity of both C@SnS<sub>2</sub> and C@ SnO<sub>2</sub> are 1611.6 mAh/g, 699.8 mAh/g and 1541.5 mAh/g, 889.6 mAh/g respectively. Although the first charge and discharge capacity of the two composites are not much difference, along with the increasing of cycle numbers the charge and discharge performance of C@SnS<sub>2</sub> composites is prevailed over that of C@SnO<sub>2</sub> significantly after comparison.



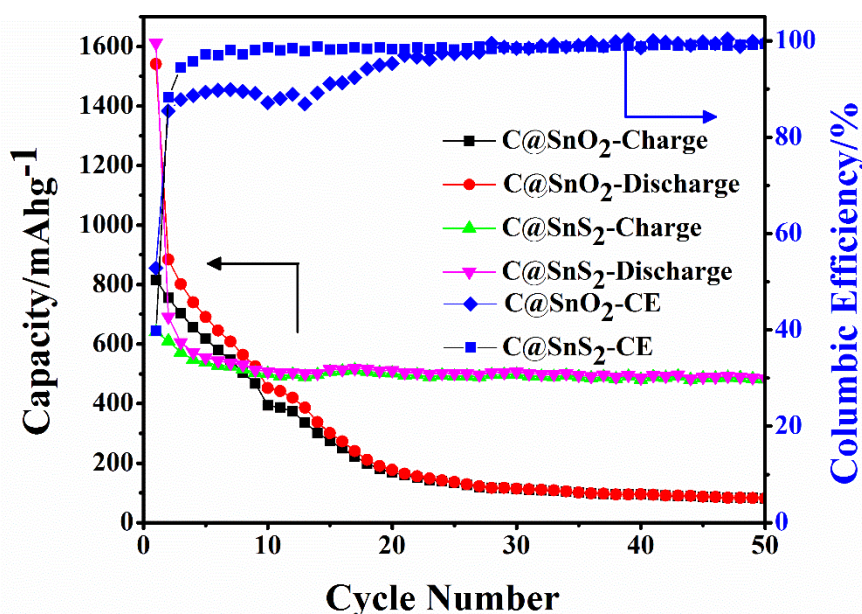
**Figure 6.** The discharge/charge profiles of C@SnS<sub>2</sub> and C@SnO<sub>2</sub> composites

Further rate performances of C@SnS<sub>2</sub> and C@SnO<sub>2</sub> composites from 0.1 to 1.5 (0.15 C=100 mA/g) are also tested as presented in Fig. 7. The discharge capacity of C@SnS<sub>2</sub> presents as large as 544.8 mAh/g at 0.1 C rate, and it exhibits first reversible capacities of 460.7 mAh/g, 392.08 mAh/g, 199.22 mAh/g, 106.16 mAh/g at 0.3, 0.5, 1 and 1.5 C, respectively. Importantly, when the current density changes back to 0.1 C, the C@SnS<sub>2</sub> composites can recover up to 536.5 mAh/g. Nevertheless, the C@SnO<sub>2</sub> composites exhibit a worse rate performance. From rate capabilities pattern of C@SnO<sub>2</sub> composites as we can see, although C@SnO<sub>2</sub> composites as the electrode materials possess high discharge capacity (862.9 mAh/g) at 0.1C, the discharge capacity was attenuated quickly as high as 284.6mAh/g after five cycles. As the rate increases, the special capacity will decrease. When the rate increases to 1.5 C, discharge capacity only remains 5.4 mAh/g, which explains the discharge and charge capacity of C@SnO<sub>2</sub> in large rate wasn't much ideal.



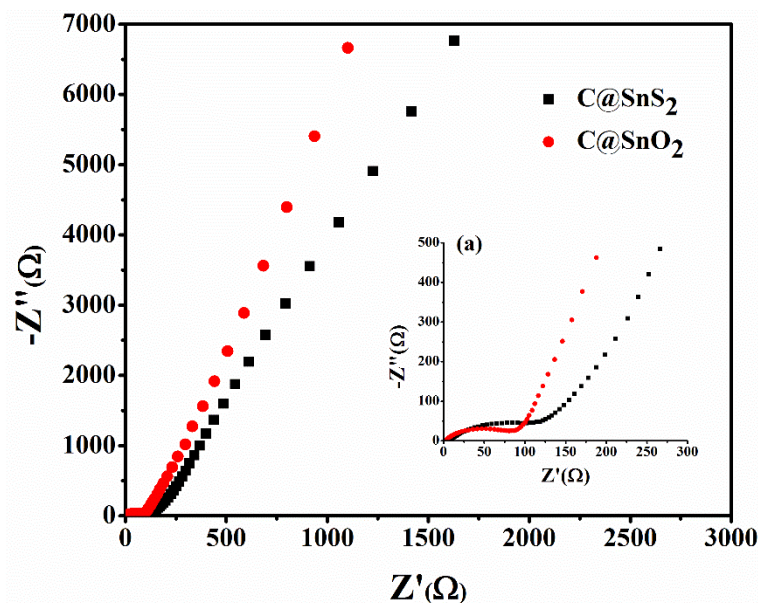
**Figure 7.** The rate capacity of C@SnS<sub>2</sub> and C@SnO<sub>2</sub> composites

Fig. 8 presents the cyclic performance and coulombic efficiencies of the C@SnS<sub>2</sub> and C@SnO<sub>2</sub> composites at a current density of 100 mA/g in the voltage window of 0.01 V-3 V for 50 cycles. As shown in Fig. 8, the cyclic performance of C@SnS<sub>2</sub> is significantly advanced than C@SnO<sub>2</sub>. The discharge/charge capacity of C@SnS<sub>2</sub> as anode material in LIBs has remained around 500 mAh/g and the coulomb efficiency is above 98% since the fifth cycle. However, the C@SnO<sub>2</sub> anode materials exhibited poor cycling performance with the reversible capacity of below 100 mAh/g after 50 cycles due to the damage of C@SnO<sub>2</sub> structure. Although the coulomb efficiency of C@SnO<sub>2</sub> as the electrode reached 98% after 20 cycles, the poor reversible capacity cannot satisfy the demand of practical electrochemical energy device. The analysis indicates that the C@SnS<sub>2</sub> composites show better cycling performance because the C@SnS<sub>2</sub> composites have better core-shell structural stability than C@SnO<sub>2</sub>.



**Figure 8.** Capacity and Coulomb efficiency versus cycle number for the C@SnS<sub>2</sub> and C@SnO<sub>2</sub> composites

The electrochemical impedance spectroscopy (EIS) tests are executed to further investigate the reactions occurred during the charge and discharge [41]. The Nyquist plots of the core-shell C@SnS<sub>2</sub> and C@SnO<sub>2</sub> anode materials are presented in Fig. 9, respectively. In the Nyquist plots, the semicircle consists of the charge-transfer resistance and the slope line in low-frequency is located at the lithium ion diffusion resistance [42]. Distinctly, the semicircle diameter of the C@SnO<sub>2</sub> anode materials is minor than the C@SnS<sub>2</sub> anode materials in Fig. 9. The appearance illustrates the C@SnO<sub>2</sub> composites as the electrode favor the electron transfer compared with C@SnS<sub>2</sub>. These results may be attributed to the increase the graphitization degree of the Cs after calcination. Furthermore, the oblique line with a large tilt angle explicates SnO<sub>2</sub> nanoparticles which formed core-shell structure provide more active sites and transfer channel of lithium ion insertion/deinsertion in active material. This result identifies with the experimental consequences shown in Fig. 6, in which the charge/discharge capacity of C@SnO<sub>2</sub> composites is significantly higher than C@SnS<sub>2</sub> in the first several cycles.



**Figure 9.** Nyquist plots of the C@SnS<sub>2</sub> and C@SnO<sub>2</sub> composites (a) Nyquist plots of the C@SnS<sub>2</sub> and C@SnO<sub>2</sub> composites in high frequency

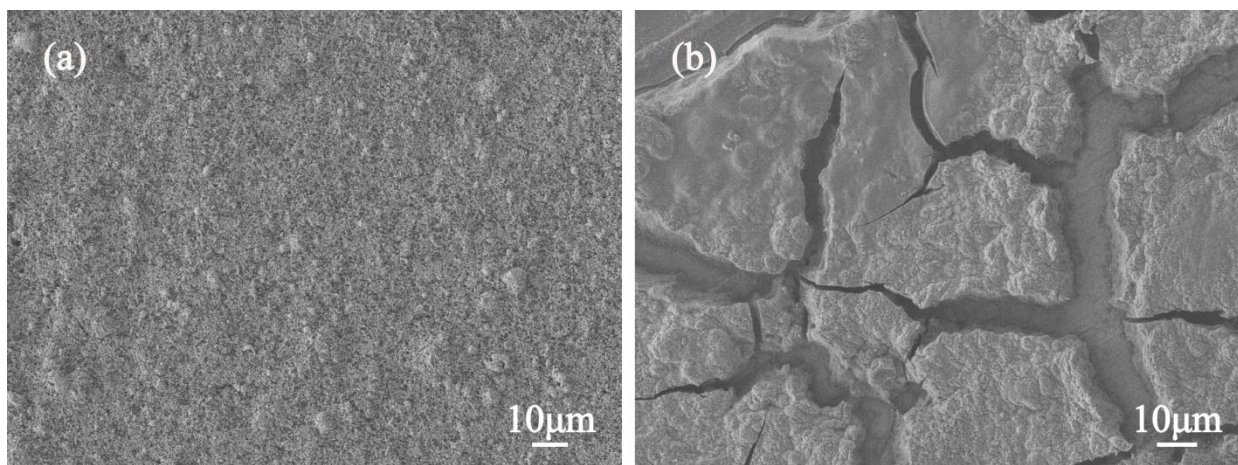


**Figure 10.** The structure of C@SnO<sub>2</sub> composites before and after 50 cycles (a) before (b) after

Above, the products were analyzed by XRD, SEM and TEM respectively, as was discovered that core-shell C@SnS<sub>2</sub> and C@SnO<sub>2</sub> composites were perfectly fabricated by one-step solvothermal method and calcination, and the further study of EIS showed that C@SnO<sub>2</sub> had higher conductivity and smaller lithium ion transfer impedance compared with C@SnS<sub>2</sub>. Unfortunately, when putting the products as anode materials for LIBs, we found that C@SnO<sub>2</sub> showed poor circulation, charge-discharge performance and rate performance. Therefore, the morphology changes of C@SnO<sub>2</sub> composites and after 50 cycles we further investigated as shown in Fig. 10. It is obviously shown in Fig. 10(a) that the morphology without cycle presents a complete film shape without any cracks. However, after 50 cycles the C@SnO<sub>2</sub> composites were completely destroyed, which the surface of the

electrode emerged a great deal of cracks and part of active materials had been detached from the surface of the current collector. The analysis indicates that those problems are directly attributable to the structural stability of the core-shell C@SnO<sub>2</sub> composites as well as lead to the poor energy storing capacity of the C@SnO<sub>2</sub> in LIBs.

#### 4. CONCLUSION

In summary, the core-shell structure C@SnM<sub>2</sub> (M=O, S) products were developed through a facile, convenient, environmental friendly method. Both two composites are formed with carbon microspheres as the core and the SnM<sub>2</sub> as the shell. When putting it as the anode materials for lithium-ion batteries, the performances of the C@SnS<sub>2</sub> composites are superior to the C@SnO<sub>2</sub>. Although the lithium storage properties of both two core-shell structure composites are not particularly excellent, it can provide a new way of thinking for other materials to synthesize the similar core-shell structure in the subsequent research.

#### ACKNOWLEDGEMENTS

The project was supported by the Key Research Projects in Gansu Province (No. 17YF1GA020).

#### References

1. M. Zhao, Q. Zhao, J. Qiu, H. Xue and H. Pang, *Rsc. Adv.*, 6 (2016) 95449.
2. H. S. Kim, Y. H. Chung, S. H. Kang and Y. E. Sung, *Electrochim. Acta*, 54 (2009) 3606.
3. Q. H. Wang, D. W. Wang, M. H. Wu, B.X. Liu, J. T. Chen, T. M. Wang and J. Chen, *J. Phys. Chem. Solids*, 72 (2011) 630.
4. Y. F. Zhu, Y. H. Chu, J. H. Liang, Y. S. Li, Z. L. Yuan, W. T. Li, Y. Q. Zhang, X. X. Pan, S. L. Chou, L. Z. Zhao and R. H. Zeng, *Electrochim. Acta*, 190 (2016) 843.
5. H. Mukaibo, A. Yoshizawa, T. Momma and T. Osaka, *J. Power Sources*, 119 (2003) 60.
6. Y. Li, J. P. Tu, X. H. Huang, H. M. Wu and Y. F. Yuan, *Electrochem. Commun.*, 9 (2007) 49.
7. H. S. Kim, Y. H. Chung, S. H. Kang and Y.E. Sung, *Electrochim. Acta*, 54 (2009) 3606.
8. Y. Zou and W. Yong, *Chem. Eng. J.*, 229 (2013) 183.
9. X.J. Hou, X.F. Wang, B. Liu, Q.F. Wang, Z.R. Wang, D. Chen and G.Z. Shen, *ChemElectroChem.*, 1 (2014) 108.
10. L. Yue, J. J. Ge, G. X. Luo, K. T. Bian, C. Yin, R. F. Guan, W. H. Zhang, Z. Zhou, K. X. Wang and X. F. Guo, *J. Electron. Mater.*, 47 (2018) 2545.
11. S. J. Han, B. C. Jang, T. Kim, S. M. Oh and T. Hyeon, *Adv. Funct. Mater.*, 15 (2005) 1845.
12. Y. Fukai, Y. Kondo, S. Mori and E. Suzuki, *Electrochem. Commun.*, 9 (2007) 1439.
13. M. Law, D. J. Sirbuly, J. C. Johnson, J. Goldberger, R. J. Saykally and P. Yang, *Science* 305 (2004) 1267.
14. H.M. Yang, G.G. Yu and H.W. Liu, *J. Electron. Mater.*, 44 (2015) 3744.
15. S. Mathur, S. Barth, H. Shen, J. C. Pyun and U. Werner, *Small*, 1 (2005) 713.
16. J. Li, J. Guo, X. Zhang and R. Peng, *Ionics*, 22 (2016) 2307.
17. Y. Chen, Q. Z. Huang, J. Wang, Q. Wang and J. M. Xue, *J. Mater. Chem.*, 21 (2011) 17448.
18. F. Han, W. C. Li, M. R. Li and A. H. Lu, *J. Mater. Chem.*, 22 (2012) 9645.
19. B. Liu, M. H. Cao, X. Y. Zhao, Y. Tian and C. W. Hu, *J. Power Sources*, 54 (2013) 243.
20. Y. Wang, F. B. Su, J. Y. Lee and X. S. Zhao, *Chem. Mater.*, 18 (2006) 1347.
21. H. W. Bai, Z. Y. Liu and D. D. Sun, *J. Mater. Chem.*, 22 (2012) 24552.

22. B. T. Zhao, S. M. Jiang, C. Su, R. Cai, R. Ran, M. O. Tade and Z. P. Shao, *J. Mater. Chem. A*, 1 (2013) 12310.
23. T. Zhu, J. S. Chen and X. W. Lou, *J. Phys. Chem. C*, 115 (2011) 9814.
24. Y. Ma, C. Zhang, G. Ji and J. Y. Lee, *J. Mater. Chem.*, 22, (2012) 7845.
25. J. Chen, X. H. Xia, J. P. Tu, Q. Q. Xiong, Y. X. Yu, X. L. Wang and C. D. Gu, *J. Mater. Chem.*, 22 (2012) 15056.
26. Y. T. Zhong, X. Wang, K. C. Jiang, J. Y. Zheng, Y. G. Guo, Y. Ma and J. N. Yao, *J. Mater. Chem.*, 21 (2011) 17998.
27. X. H. Huang, J. P. Tu, C. Q. Zhang, X. T. Chen, Y. F. Yuan and H. M. Wu, *Electrochim. Acta*, 52 (2007) 4177.
28. X. H. Huang, J. P. Tu, C. Q. Zhang and J. Y. Xiang, *Electrochim. Acta*, 9 (2007) 1180.
29. X. J. Chen, G. Y. Yu, A. S. Wang and H. Li, *J. Lanzhou Univ. of Tech.*, 44 (2018) 6.
30. C. D. Wood, B. Tan, A. Trewin, H. Niu, D. Bradshaw, M. J. Rosseinsky, Y. Z. Khimyak, N. L. Campbell, R. Kirk, E. Stocket and A. I. Cooper, *Chem. Mater.*, 19 (2007) 2034.
31. J. S. Song, F. Tronc and M. A. Winnik, *J. Am. Chem. Soc.*, 126 (2004) 6562.
32. C. Zou, D. C. Wu, M. Z. Li, Q. C. Zeng, F. Xu, Z. Y. Huang and R. W. Fu, *J. Mater. Chem.*, 20 (2010) 731.
33. Q. Y. Hao, D. N. Lei, X. M. Yin, M. Zhang, S. Liu, Q. H. Li, L. B. Chen and T. H. Wang, *J. Solid State Electr.*, 15 (2011) 2563.
34. Y. Zhao, D. L. Gao, J. F. Ni, L. J. Gao, J. Yang and Y. Li, *Nano Res.*, 7 (2014) 765.
35. Q. Z. Wang, J. H. Lian, Q. Ma, S. L. Zhang, J. J. He, J. B. Zhong, J. Z. Li, H. H. Huang and B. Su, *Catal. Today*, 281 (2017) 662.
36. Q. H. Wang, D. W. Wang, M. H. Wu, B. X. Liu, J. T. Chen, T. M. Wang and J. Chen, *J. Phys. Chem. Solids*, 72 (2011) 630.
37. W. N. Deng, X. H. Chen, Z. Liu, A.P. Hu, Q. L. Tang, Z. Li and Y. N. Xiong, *J. Power Sources*, 277 (2015) 131.
38. L. X. Yin, S. M. Chai, J. F. Huang, X. G. Kong and L. M. Pan, *Electrochim. Acta*, 238 (2017) 168.
39. H.Y. Sun, M. Ahmad, J. Luo, Y.Y. Shi, W.C. Shen and J. Zhu, *Mater. Res. Bull.*, 49 (2014) 319.
40. P. L. Zheng, Z. F. Dai, Y. Zhang, K. N. Dinh, Y. Zheng, H. S. Fan, J. Yang, R. Dangol, B. Li, Y. Zong, Q. Y. Yan and X. B. Liu, *Nanoscale*, 9 (2017) 14820.
41. W. W. Xu, Z. Q. Xie, X. D. Cui, K. N. Zhao, L. Zhang, L. Q. Mai and Y. Wang, *J. Mater. Chem. A*, 4 (2016) 3735.
42. S.M. Hwang, Y. G. Lim, J. G. Kim, Y. U. Heo, J. H. Lim, Y. Yamauchi, M. S. Park, Y. J. Kim, S. X. Dou and J. H. Kim, *Nano Energy*, 10 (2014) 53.